Research Article

Local chemical inhomogeneities in TiZrNb-based refractory high-entropy alloys

Kaihui Xun [a,1], Bozhao Zhang [a,1], Qi Wang [b,1], Zhen Zhang [a], Jun Ding [a,*], En Ma [a,*]

[a] *Center for Alloy Innovation and Design (CAID), State Key Laboratory for Mechanical Behavior of Materials, Xi'an Jiaotong University, Xi'an 710049, China*
[b] *Science and Technology on Surface Physics and Chemistry Laboratory, P. O. Box 9-35, Jiangyou 621908, China*

ABSTRACT

Multi-principal element solid solutions are prone to develop local chemical inhomogeneities, *i.e.*, chemical order/clustering and/or compositional undulation. However, these structural details from short-range (first couple of nearest-neighbor atomic shells) to nanometer length scale are very challenging to resolve in both experimental characterization and computer simulations. For instance, Monte Carlo modeling based on density-functional-theory calculations is severely limited by the sample size and the simulation steps practical in the simulations. Adopting the cluster expansion approach, here we systematically reveal the local chemical inhomogeneity, including chemical order and compositional fluctuation, in three representative equiatomic TiZrNb-based body-centered cubic refractory high-entropy alloys (HEAs): TiZrNb, TiZrHfNb and TiZrHfNbTa. Ti-Zr pairs are found to exhibit the highest degree of chemical preference among all atomic pairs. Such chemical short-range order (CSRO) induces an accompanying compositional undulation, both extending to characteristic dimensions of the order of one nanometer. The chemical inhomogeneity trend uncovered for this series of TiZrNb-based HEAs is expected to impact their mechanical properties; *e.g.*, incorporating the CSRO effects in a current model significantly improves its agreement with experimental measured yield strength.

© 2022 Published by Elsevier Ltd on behalf of The editorial office of Journal of Materials Science & Technology.

1. Introduction

High-entropy alloys [1–4] (HEAs) composed of multiple principal elements in equimolar or near-equimolar proportions have attracted substantial research interest in recent years. These HEAs are often based on single-phase solid solutions with face-centered cubic (fcc), body-centered cubic (bcc), or hexagonal-close packed (hcp) structures. Among them, bcc HEAs containing refractory metal elements have been projected to be promising candidates for high-temperature structural applications. A family of bcc refractory HEAs of special interest are those containing Zr and/or Hf, such as TiZrNb [5,6], TiZrHfNb [7,8], TiZrHfNbTa [9–12], ZrHfNbTa [13,14], TiZrHfTa [15], and HfNbTa [16]. These bcc HEAs usually exhibit a good balance of strength and ductility, a desirable trait absents from other bcc refractory HEAs that are very strong but rather brittle. For example, TiZrHfNbTa HEA [17] possesses high mechanical strength ($\sigma_{0.2} = 929$ MPa) and good compression plasticity ($\varepsilon >$ 50%). Recently, Wei et al. [18] designed a $Ti_{38}V_{15}Nb_{23}Hf_{24}$ refrac-

tory HEA and achieved near-GPa strength and >20% tensile ductility in the as-cast state.

In terms of structural details, the TiZrNb-based bcc HEAs also stand out among all the HEAs, for the following two reasons. First, their lattice often exhibit severe local distortion [19,20], due to the relatively large atomic size differences among the principal elemental species making up the alloy, even to the extent of breaking the 15% size difference limit expected for single-phase solutions (the Hume-Rothery rule). Such severe local lattice distortion can significantly influence the thermodynamic stability, microstructure, deformation mechanisms, and other properties. Second, due to the varying chemical affinity among the species in these TiZrNb-based bcc HEAs, they are more prone to local chemical order (LCO) [7] when compared with other recently studied HEAs (*e.g.*, the fcc ones such as NiCoCr [21–24], NiCoV [25], and NiCoCrFePd [26]). In other words, in contrast to random solid solution (RSS) approaching an ideal solution, where the constituent elements uniformly distribute on the lattice sites, the TiZrNb-based bcc HEAs are likely to develop LCO, which adds another variable that can be exploited to tailor their properties. In addition to such chemical ordering of the principal elements, the LCO can be enhanced by adding solutes that exhibit strong chemical affinity with some of the constitute
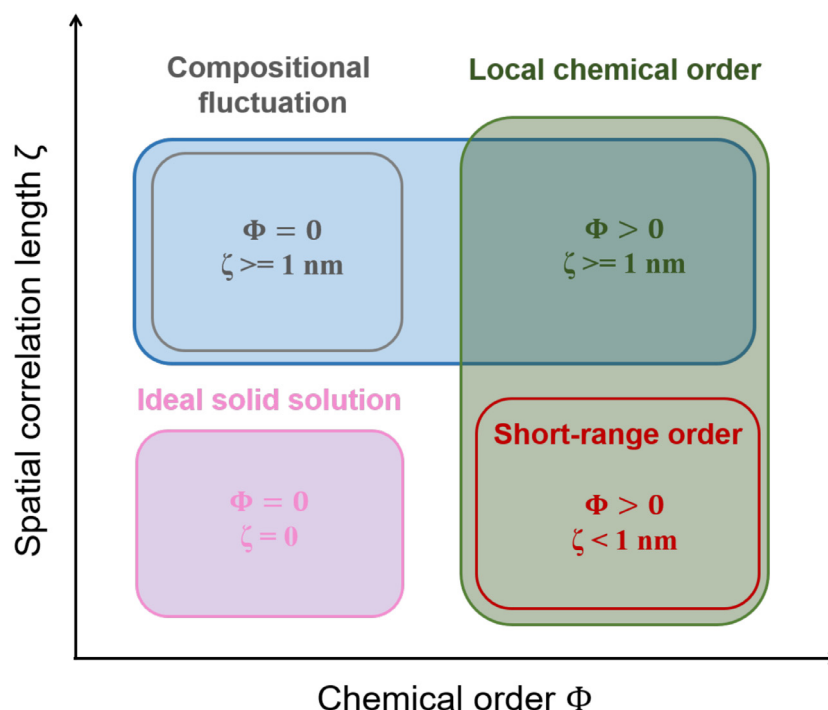

Fig. 1. Illustration of local chemical inhomogeneity using the chemical order parameter (Φ) and spatial correlation length (ξ). Φ is a parameter to describe the degree of chemical order and ξ denotes the characteristic length of the local chemical inhomogeneity.

species. For example, Lei et al. [8] purposely doped their TiZrHfNb HEA with 2 at.% oxygen to form ordered (Zr, Ti)-enriched oxygen complexes. Such additional LCOs can markedly alter the dislocation glide mode, *e.g.*, from planar slip to double-cross slip, hence causing a simultaneous increase in tensile strength and ductility. Pang et al. [27] also reported a similar approach to achieve the strength-ductility synergy in TiZrNb HEAs via boron doping.

The current paper focuses on the local chemical inhomogeneities existing in TiZrNb-based solid solutions. In general terms, the chemical inhomogeneity has two distinct but often closely related aspects: local chemical order (which, as outlined above, can be a prominent feature in these HEAs) and compositional undulation [28,29]. The incipient form of LCO is the chemical short-range order, CSRO, which describes the partial chemical order (including in some cases tendency towards clustering of one of the constituent elements) in the first couple of nearest-neighbor atomic shells. On the other side of the spectrum, LCO can also be developed to the extent of superlattice structures with domain size on the order of (many) nanometers, as known for the precipitates of intermetallic compound (nano)crystals. In the discussion below, our focus is to examine systematically the LCO in the range from CSRO to one nanometer length scale. The compositional undulation, on the other hand, refers to the spatial variation of chemical concentration, *e.g.*, in the form of incipient concentration waves that have a correlation length beyond the nanometer scale typical of statistical compositional fluctuation (which is expected when the local regions being examined are extremely small). These two characteristic structural features in a concentrated solid solution are schematically illustrated in Fig. 1 using the chemical order parameter (Φ) and spatial correlation length (ξ) [30]. Φ is a virtual parameter to describe the degree of chemical order within the range of 0 to 1, where the value of 0 refers to RSS and the value of 1 is for the highest degree of chemical order. ξ describes the characteristic length of the local chemical inhomogeneity. Note that alloys with (local) chemical order do not necessarily exhibit composition variation; an example is the ordered $L1_2$ Ni_3Al intermetal-

lic precipitates. Additionally, alloys with compositional undulation do not have to be chemically ordered (see the NiCo alloy in Ref. [31] and NiCoCrFePd HEA in Ref. [26]). However, in many cases, both local chemical order and compositional fluctuation coexist (see MD-simulated NiCoCr alloy in Ref. [32], where the tendency towards LCO eventually leads to the formation of nanometer-sized domains that differ in local composition).

We reiterate that an appreciable degree of chemical inhomogeneity is expected in any given Zr- and/or Hf-containing bcc HEA, because the constituent elements have relatively large atomic size mismatch and difference in electronegativity. Specifically, TiZrHfNb alloy, as a representative case, has been directly demonstrated [8] to contain (Hf,Nb)-rich and (Ti,Zr)-rich nanoscale regions ($\sim$ 1-2 nm) from the three-dimensional reconstruction of atom probe tomography (APT) data. In addition, our previous density-function-theory (DFT)-based Monte Carlo (MC) simulations of TiZrHfNb [33] demonstrated the presence of CSRO for the first (nearest neighbor) NN shell using a limited size of configurations (100–200 atoms) and preliminary MC simulations (4000 swap steps). The simulated sample size and MC steps are intrinsically limited by the very expensive computational costs for DFT calculations. Apparently, such small-scale atomistic simulation results are still far detached from the experimental observation, especially in terms of the characteristic length scale of local chemical inhomogeneity. In other words, the current challenge for clarifying the local chemical inhomogeneity in the TiZrHfNb alloy is two-fold: (i) so far there has been no direct observation of the local chemical order via experimental characterization; (ii) DFT-based MC simulation can only predict the local chemical order in the first NN shell, *i.e.*, CSRO. To circumvent this problem, the approach of hybrid MC and molecular dynamics simulation utilizing empirical interatomic potential is a possibility. However, an accurate and robust interatomic potential for this quaternary alloy system is still not available.

In this work, we carried out a systematic cluster expansion (CE) approach to examine the local chemical inhomogeneity in TiZrNb-based bcc refractory HEAs (*i.e.*, TiZrNb, TiZrHfNb, and TiZrHfNbTa).

The CE approach is based on the Hamiltonian describing the crystal configuration energy and has a very high computational efficiency for multicomponent materials. By implementing MC simulation based on the CE approach, we reveal the evolution of local chemical inhomogeneities, including the development of LCO and the accompanying compositional undulation, from the chemically disordered structure at high temperatures to the strong tendency of forming different chemically favored pairs, even reaching a characteristic length of nanometer scale at lower temperatures. Our results provide useful information for guiding the structure-property design of bcc refractory HEAs, in particular for this TiZrNb-based sub-group that offers ample opportunities for employing LCO to tune alloy properties.

2. Methods

2.1. Cluster expansion (CE) approach

In the cluster expansion approach, crystalline materials are modeled using a generalized Ising model in which various multi-body cluster interaction terms called effective cluster interactions (ECI) [34] must be determined. A configuration $\vec{\sigma}$ with M different species can be expressed by the occupation variables of integer σ_i, which denotes the kind of atom is on atomic lattice point i. Typically, the value of σ_i can be taken from 0 to $M_i - 1$ (*e.g.* for quaternary alloy ($M = 4$), σ_i could be 0, 1, 2, 3). The energy of configuration $\vec{\sigma}$ is represented by different ECIs as the following formula:

$$\Delta H_{\mathrm{mix}}\left(\vec{\sigma}\right) = \sum_{\omega} J_{\omega} m_{\omega} \langle \Gamma_{\omega'}\left(\vec{\sigma}\right) \rangle_{\omega} \tag{1}$$

where ω denotes a cluster, generally expressed as a vector, and ω_i is an element of vector ω, representing the atomic species on lattice site i, with values from 0 to $M_i - 1$. m_{ω} denotes the multiplicity of ω clusters, which is equivalent to ω by symmetry. J_{ω} are the effective cluster interactions corresponding to cluster ω. Cluster functions, $\langle \Gamma_{\omega'}(\vec{\sigma}) \rangle_{\omega}$ are defined as the product of point functions occupying positions on a particular cluster ω. Its expression corresponding to the multi-component alloy system is [35]

$$\langle \Gamma_{\omega}(\vec{\sigma}) \rangle = \prod_{i} \gamma_{\omega_i, M_i}(\sigma_i). \tag{2}$$

In this work, we use the Python package *icet* [36] for training to obtain the corresponding ECIs, J_{ω}. The point functions $\gamma_{\omega_i, M_i}(\vec{\sigma}_i)$ are based on the van de Walle's method [35,37–39]:

$$\gamma_{\omega_i, M_i}\left(\Rightarrow \sigma_i\right) = \begin{cases} 1 & \text{if } \omega_i = 0 \\ -\cos\left(\pi \frac{\omega_i \sigma_i}{M}\right) & \text{if } \omega_i > 0 \text{ and odd}, \\ -\sin\left(\pi \frac{\omega_i \sigma_i}{M}\right) & \text{if } \omega_i > 0 \text{ and even}. \end{cases} \tag{3}$$

2.2. Dataset for CE fitting

The dataset for cluster expansion training is obtained from the DFT calculation, as illustrated in Fig. 2. The DFT calculation package, Vienna *ab initio* Simulation Package [40–42], was used to calculate the configurational energy of 500 independent $4 \times 4 \times 4$ supercells (each containing 128 atoms) for TiZrNb, TiZrHfNb and TiZrHfNbTa, individually. Projection-enhanced waves (PAW) [43] are employed to describe the electron-ion interactions. The k-point mesh ($3 \times 3 \times 3$) in the Brillouin region is set by the Monkhorst-Pack method [42]. The exchange-correlation function is a generalized gradient approximation (GGA) parameterized by Perdew-Burke-Ernzerhof (PBE) [44]. The cutoff energy of plane waves was determined to be 380 eV after the convergence test, and the self-consistent convergence criterion is that the total energy is less than 4.0×10^{-5} eV/atom.

2.3. CE-based MC simulation

The MC simulation method was applied for simulated annealing of the TiZrNb-based HEAs. Equimolar alloy samples with 2880 atoms and dimensions of $12 \times 12 \times 10$ unit cells (corresponding to 4.1 nm $\times$ 4.1 nm $\times$ 3.4 nm) were generated, and the atoms then randomly placed onto lattice positions to serve as the initial structure for the simulated annealing. For each configuration and each desired MC temperature, T_{MC}, the MC simulation was run for a total of 600,000 steps, which corresponds to approximately 210 exchange trials per atom. The CE approach predicts the energy of the post-simulation configuration at each step, which is used to determine if the exchange at this step is accepted. The MC method was implemented by a Python compilation and combined with CE for conformational energy prediction of these TiZrNb-based HEAs. The process is as follows (see also Fig. 2): (i) the conformational energy of the initial cell is predicted using CE; (ii) a new configuration is obtained by randomly exchanging two atoms in the cell, and each exchange of atoms is considered an MC step; (iii) the energy of the new configuration obtained at each MC step is predicted using CE; (iv) following the Metropolis algorithm, the probability that the new configuration is accepted is

$$P = \begin{cases} 1, & \Delta E \leqslant 0 \\ \exp\left(-\Delta E / (k_{\mathrm{B}} * T_{\mathrm{MC}})\right), & \Delta E > 0 \end{cases} \tag{4}$$

where ΔE is the amount of change in the energy of the system due to the exchange of atomic positions and $k_{\mathrm{B}} * T_{\mathrm{MC}}$ is the Boltzmann factor. The new structure, once accepted, is reused as the initial structure, and the above operation is repeated. Eventually, the energy profile and the equilibrium structure of these TiZrNb-based HEAs converge after a sufficient number of MC steps.

2.4. DFT-based MC simulation

A DFT-based lattice MC approach was employed for TiZrNb, TiZrHfNb and TiZrHfNbTa alloys. The initial starting point of the MC simulations adopted an equimolar $5 \times 5 \times 5$ supercell, containing 250 atoms, which was generated as a special quasi-random structure (SQS) [45]. Similar to the method in previous literature [23,33,46], MC simulations were run for a total of 3000 steps at a MC temperature of 600 K, corresponding to approximately 10 swap trials per atom. Energy calculations after each MC swap were executed with the Vienna *ab initio* simulation package. Brillouin zone integrations were performed using Monkhorst–Pack meshes with a single k-point (Γ) with a plane wave cutoff energy of 350 eV. The PBE formalism was adopted to describe exchange and correlation interactions, and the PAW method was utilized for dealing with electron-ion interactions.

3. Results

3.1. Evaluation of the cluster expansion model

The CE models for the potential energy of these TiZrNb-based alloys were trained using 500 independent supercells (with $4 \times 4 \times 4$ unit cells, containing 128 atoms) in equal molarity. The ECI parameters for the CE models are fitted directly through the Python third-party library *icet* [36]. The fitting accuracy of the ECI parameters needs to be scrutinized to ensure the predictive power of our CE models for the cohesive energies (related to potential energy) of TiZrNb-based HEAs. The cohesive energy typically reflects the stability of the atomic configuration, which is defined as the difference between the energy of alloy and the sum of the corresponding isolated atomic energies:

$$E_{\mathrm{coh}} = \frac{1}{N}\left(E_{\mathrm{alloy}} - \sum n_i E_i\right) \tag{5}$$
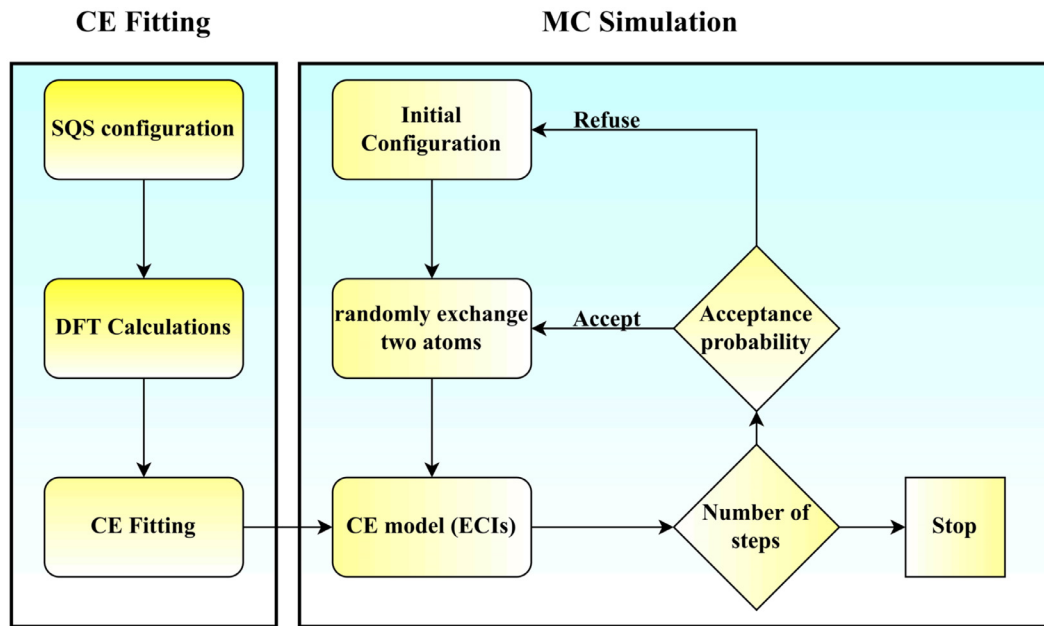
CE Fitting

MC Simulation

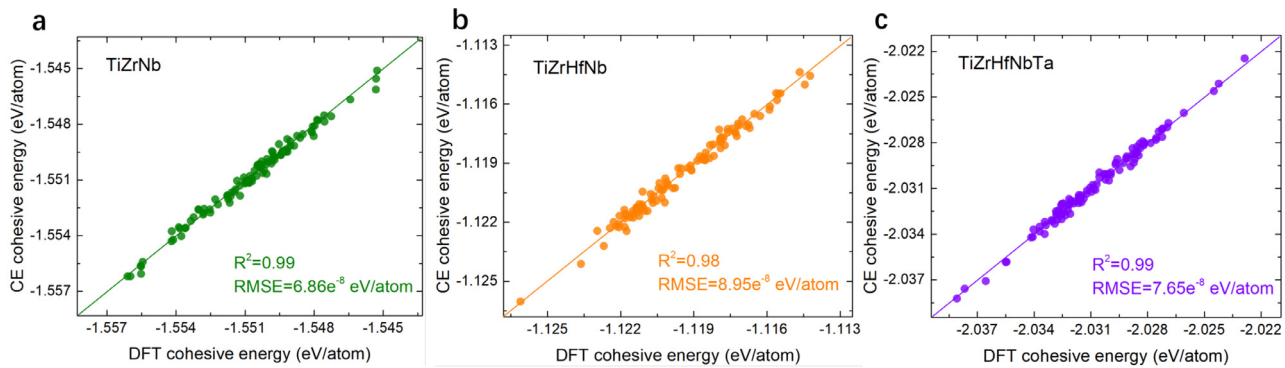**Fig. 2.** Flowchart of CE fitting and MC simulations.

Fig. 3. Generalization ability of the fitted CE models by comparing CE-predicted and DFT-calculated cohesive energy for (a) TiZrNb, (b) TiZrHfNb, and (c) TiZrHfNbTa HEAs

Here, $E_{\mathbf{alloy}}$ is the total energy of the alloy system. E_i and n_i represent the energy and number of isolated atoms of species i, respectively. N denotes the total number of atoms in the alloy system. The correlation coefficient (R^2) and root mean square error (RMSE) are often utilized as judging criteria when assessing the predictive accuracy of models based on regression analysis, *i.e.*, generalization ability:

$$R^2 = 1 - \frac{\sum_{i=1}^{N} \left(y_i - y'_i\right)^2}{\sum_{i=1}^{N} \left(y'_i - \bar{y}\right)^2} \tag{6}$$

$$\text{RMSE} = \sqrt{\frac{1}{N} \sum_{i=1}^{N} \left(y_i - y'_i\right)^2} \tag{7}$$

where y_i, y'_i and $\bar{y}$ denote the actual value, the predicted value and the averages of the actual values, respectively. The closer to unity the correlation coefficient R^2 is, the better the fitting achieved via the model.

Then, 100 additional samples for TiZrNb, TiZrHfNb, and TiZrHfNbTa each were assigned for prediction evaluation. Fig. 3 demonstrates the excellent generalization ability of our CE models applied to all three TiZrNb-based alloys by comparing the CE-predicted and DFT-calculated cohesive energies. In particular, the prediction data points are almost uniformly distributed

in close proximity to the y = x line (see Fig. 3(a–c)), with RMSE = 6.86×10^{-8}, 8.95×10^{-8}, and 7.65×10^{-8} eV/atom for TiZrNb, TiZrHfNb, and TiZrHfNbTa, respectively. Moreover, their corresponding R^2 values are respectively 0.99, 0.98, and 0.99, indicating a very high accuracy of the CE models.

3.2. MC temperature dependence of the cohesive energies

CE-based MC simulations were applied on three equimolar TiZrNb-based samples with 2880 atoms to achieve convergence at each MC temperature, spanning from $T_{\mathrm{MC}} = 400$ K to 1800 K. Fig. 4 depicts the cohesive energy of the final MC configurations, *i.e.*, the energetically favorable atomic configurations at different T_{MC}. The lower the T_{MC} is, the lower the cohesive energy for the annealed configuration. From the RSS configuration to the configuration with the lowest annealing temperature, the reduction in cohesive energy per atom is 0.02 eV for TiZrNb, 0.033 eV for TiZrHfNb, and 0.026 eV for TiZrHfNbTa, respectively. It is worth noting that their cohesive energies drop sharply when T_{MC} goes below a critical temperature, which is $\sim$ 600 K, 750 K and 700 K for TiZrNb, TiZrHfNb and TiZrHfNbTa, respectively (see Fig. 4(a–c)), suggesting an order-disorder transition resulting in pronounced chemical inhomogeneity. This will be discussed in detail in the following sections.
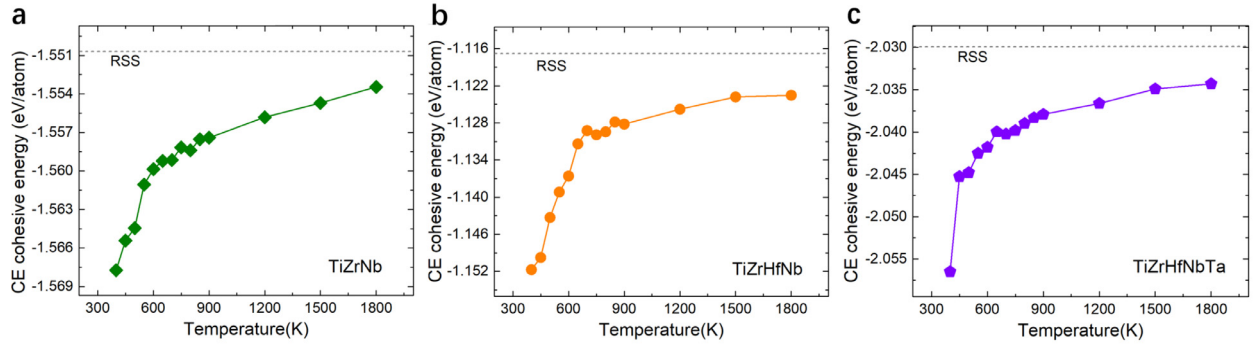
Fig. 4. Cohesive energy for the final configurations from CE-based MC simulation for (a) TiZrNb, (b) TiZrHfNb and (c) TiZrHfNbTa HEAs, over the range of MC temperatures simulated.
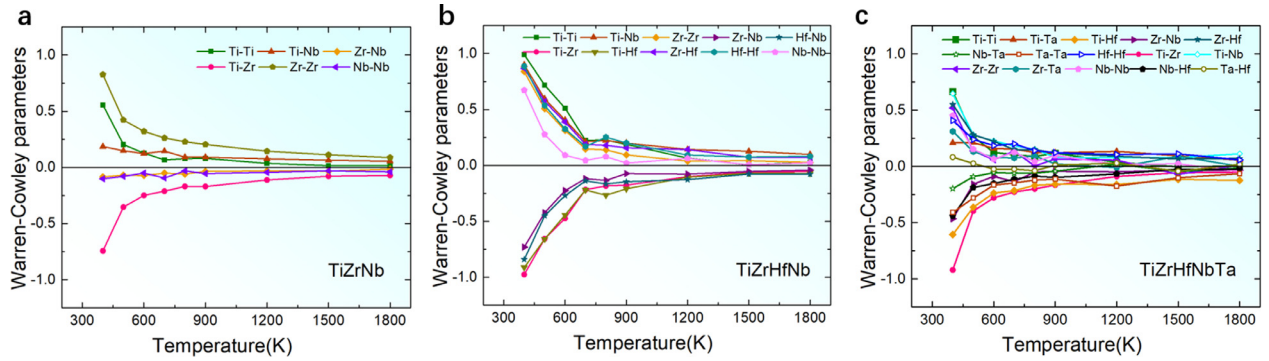

Fig. 5. Temperature dependence of Warren–Cowley parameters δ_{ij} among different pairs within the first nearest-neighbor shell for (a) TiZrNb, (b) TiZrHfNb and (c) TiZrHfNbTa alloy from CE-based MC simulation.

3.3. Chemical inhomogeneity in TiZrNb-based HEAs

The temperature dependence of CSRO (*i.e.*, 1st NN shell) from CE-based MC simulations are presented in Fig. 5 for TiZrNb, TiZrHfNb and TiZrHfNbTa alloys, spanning from 400 K to 1800 K. To characterize the pair preferences in detail, we utilized the classical Warren–Cowley parameters [47] to quantify the local chemical order:

$$\delta_{ij} = 1 - \frac{N_{ij}}{NX_j} \tag{8}$$

where N_{ij} denotes the number of ***j***-type atoms in the NN shells around an *i*-type atom, *N* is the total number of atoms in the NN shells around an atom of interest, and X_j represents the corresponding concentration of type *j* in the alloy. In the case of a random alloy, $\delta_{ij} = 0$. Positive (negative) values of δ_{ij} reflect a tendency of unfavored (favored) *i-j* pairs. Fig. 5 shows the details of δ_{ij} of different pairs in the 1st NN shell. Apparently, at lower temperatures, a very strong tendency of elemental preference occurs, which can be seen from Fig. 5(a–c) that δ_{ij} deviates significantly from $\delta_{ij} = 0$ (corresponding to RSS). At high temperatures, the δ_{ij} values of all pairs approach zero. It is thus apparent that the formation of CSRO is driven by energy reduction toward more stable configurations compared to the starting RSS alloy. Note that the δ_{ij} also changes markedly below a critical temperature, corresponding to the temperature interval where the cohesive energy changes sharply in Fig. 4 for each alloy. Note that the δ_{ij} in the 1st NN is consistent with the DFT-based MC simulation at T_{MC} = 600 K in previous literature [33]. Focusing on the case of T_{MC} = 400 K, all three alloys show a very strong tendency of forming chemically favored Ti-Zr pairs, with the most negative δ_{ij} for TiZrNb, TiZrHfNb, and TiZrHfNbTa being −0.74, −0.98, and −0.92, respectively. The strong Ti-Zr pair was also captured in previous study [48] of TiZrNb by implementing hybrid MD/MC simu-

lations. This can be explained by the estimated enthalpy of mixing by Miedema's model [49], where the value for Ti-Zr pairs is ∼ 0 kJ/mol and is the lowest among all other atomic pairs in Ti-Zr-Hf-Nb-Ta. Thus, the highly favored Ti-Zr pairs can be regarded as the characteristic CSRO among TiZrNb-based HEAs in our study.

As briefly mentioned in the Introduction section, a typical drawback of DFT-based MC simulation is that only CSRO, with a length scale of a few angstroms, can be accurately captured, due to the limited size of the configurations (100–200 atoms) and preliminary MC simulations (<4000 steps). Thus, it is worth noting that our samples of 2880 atoms, obtained using CE-based MC simulations, offer the opportunity for us to describe the features of LCO and compositional fluctuation to nanometer length scale, which can be compared with experimental characterization. Thus, we next tested whether these TiZrNb-based bcc HEAs possess nanoscale elemental preference characteristics, *i.e.*, local chemical order, by analyzing the corresponding Warren-Cowley parameters δ_{ij} within the first four nearest-neighbor shells (denoted as 1-4 NN shells), *i.e.*, a surrounding region about 1.2 nm in diameter. Here, TiZrNb, TiZrHfNb and TiZrHfNbTa samples obtained from three T_{MC}, including 400 K, 600 K and 1500 K, are considered, as shown in Fig. 6. As the temperature increases, all types of pairs converge to the RSS case, indicating that chemical preferences driven by energy reduction are overwhelmed by entropy-driven randomization at high annealing temperatures. δ_{ij} within the 1-4 NN shells generally exhibits a trend generally consistent with that within the 1 NN shell, but at a weaker degree. The general LCO features for the studied TiZrNb-based alloys are as follows: (i) For the TiZrNb alloy, the Ti-Zr pair is strongly favored, whereas the tendency of forming other atomic pairs is weak; (ii) For the TiZrHfNb alloy, Ti and Nb prefer to pair with Zr and Hf; (iii) For TiZrHfNbTa, Ta is prone to forming nanoscale segregation themselves, in addition to the coexisting chemical preference among Ti, Zr, Hf and Nb.
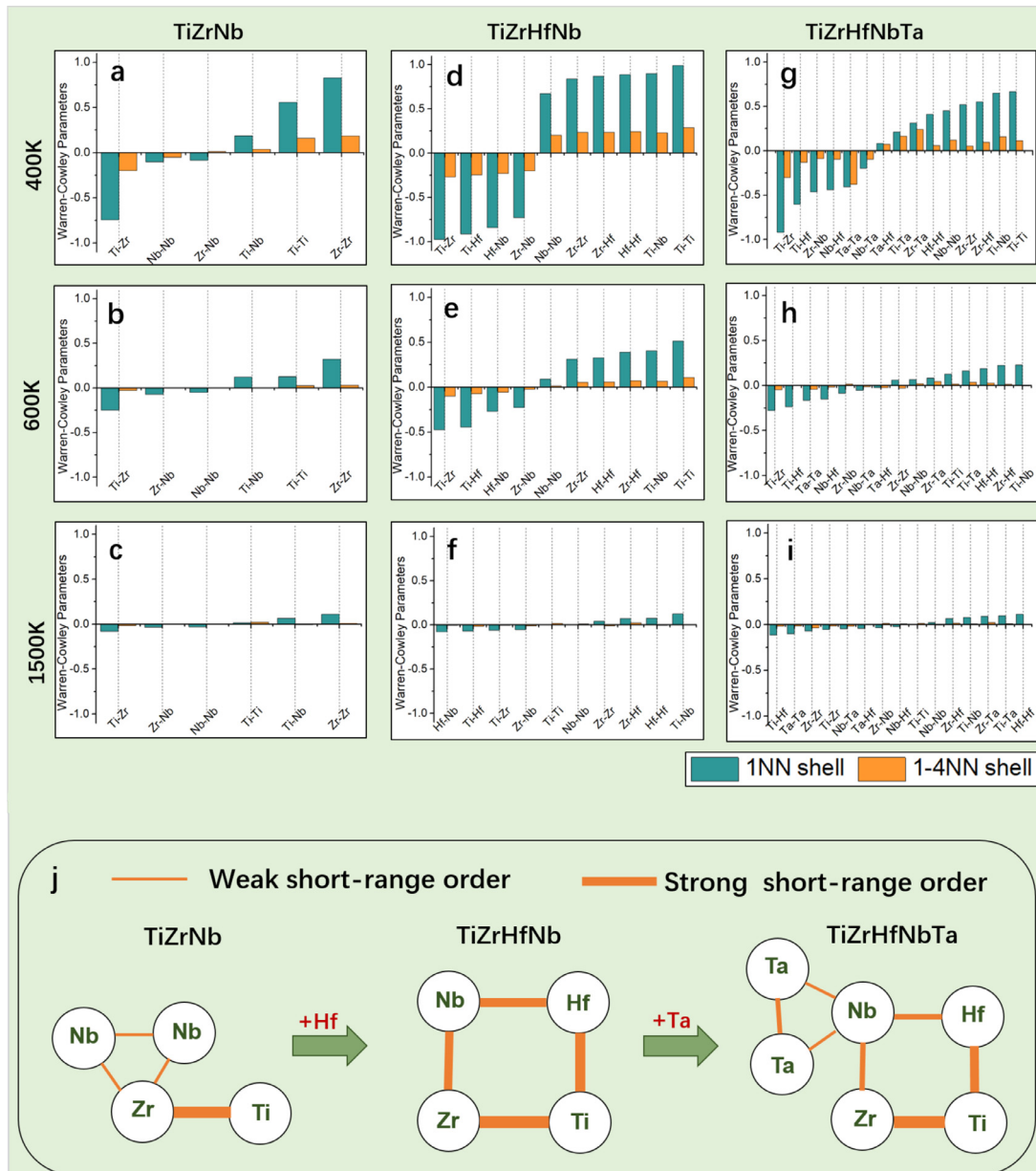
Fig. 6. Histograms of Warren-Cowley parameters δ_{ij} of (a–c) TiZrNb, (d-f) TiZrHfNb, and (g–i) TiZrHfNbTa within the 1 NN and 1-4 NN shells, at three different MC temperatures. (j) An illustration to compare the local chemical order in TiZrNb, TiZrHfNb and TiZrHfNbTa alloys. The line connecting two elements indicates the degree of chemical preference (*i.e.*, the thicker line is for the higher degree of chemical preference, and vice versa).

The formation of the CSRO (1 NN shell) and local chemical order (1-4 NN shells) are both a consequence of the competition between elements with varied chemical preferences. Ti-Zr pairs exhibit the highest preference compared to all other atomic pairs in TiZrNb, TiZrHfNb and TiZrHfNbTa alloys. For the TiZrNb alloy, the Ti-Zr pair is most favored, and Nb is unfavored to pair with Ti, resulting in less Nb-Nb and Zr-Nb pairs. This implies a degree of Nb clustering, embedded within the matrix of TiZrNb. For the TiZrHfNb alloy, the inserted Hf also favors bonding with Ti and Nb, thus resulting in the formation of (Ti, Zr)-rich and (Nb, Hf)-rich nanoscale regions, which is consistent with the three-dimensional reconstruction of atom probe tomography data [7]. In addition, they are accompanied by some weaker (Ti, Hf)-rich and (Nb, Zr)-rich regions. For TiZrHfNbTa, the introduced Ta does not form sufficiently strong chemical bonds with Ti, Zr, Hf, or Nb, so it does not perturb the local chemical order features among other elements (Ti, Zr, Hf, Nb). Fig. 6(g) shows that δ_{ij} for Ta-Ta has a value of

around -0.4 event up to the 4th NN shell, suggesting that Ta atoms are likely to form nanoscale segregation themselves. A comparison of the local chemical order in TiZrNb, TiZrHfNb and TiZrHfNbTa alloys is schematically illustrated in Fig. 6(j).

3.4. Local compositional fluctuation in TiZrHfNb alloy

In general, local chemical order and compositional fluctuations are mutually independent structural features with no required dependency between them (see illustration in Fig. 1). After revealing the local chemical order in Figs. 5 and 6, we now move on to examine the local compositional fluctuation in a representative case, the TiZrHfNb alloy. Here, we define the local composition concentration for each atom as the measured concentration value around itself using the cutoff of 8 NN shell (with a diameter of ~1.6 nm), which is close to the characteristic length (~1-2 nm) of experimentally observed clusters [7]. There is only negligible
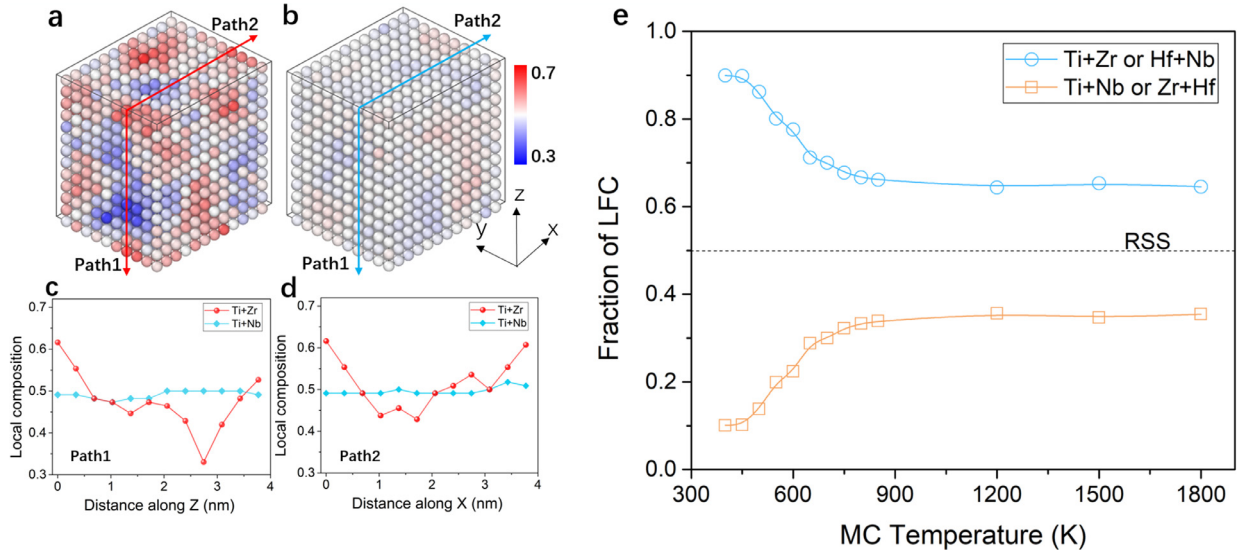
Fig. 7. Local composition (atomic molar fractions) of (a) C_{Ti+Zr} and (b) C_{Ti+Nb} in the TiZrHfNb HEA obtained from CE-based MC simulation with T_{MC} = 400 K. Two randomly selected paths along the x and z directions are denoted, and the corresponding C_{Ti+Zr} and C_{Ti+Nb} for the atoms along those paths are presented in (c) and (d). (e) f_{LFC}, defined as the fraction of locally favored compositions ([(Ti,Zr) or (Hf,Nb)] versus [(Ti,Nb) or (Hf,Zr)]), for the TiZrHfNb configurations at various MC temperatures. The concentration of 0.5 corresponds to the RSS configuration that shows a uniform distribution of elements.

local chemical order (Warrant-Cowley parameter, $|\delta_{ij}| < 0.007$) at this length scale, even for the most chemically ordered configurations in our study (annealed at the lowest temperature). Fig. 7(a, b) shows the local composition concentrations of (Ti, Zr) and (Ti, Nb), respectively (the atomic fractions are denoted as C_{Ti+Zr} and C_{Ti+Nb}), mapped over the whole CE-based MC TiZrHfNb sample (T_{MC} = 400 K). Apparently, for C_{Ti+Zr} (or equivalently 1 − C_{Hf+Nb}), there are highly fluctuating concentrations within a wide range of 0.3 – 0.7, while C_{Ti+Nb} only fluctuates weakly around the value of 0.5, which is also the value for uniform distribution of elements. Moreover, we randomly choose two paths along the x and z directions (see illustration in Fig. 7(a, b)), and the corresponding C_{Ti+Zr} and C_{Ti+Nb} along those two paths are presented in Fig. 7(c, d) to quantitatively describe the composition fluctuations. A stark contrasting behavior of C_{Ti+Zr} and C_{Ti+Nb} can be clearly observed. Furthermore, we define the fraction of locally favored clusters, f_{LFC}, by counting the possibility of ([(Ti,Zr) or (Hf,Nb)] versus [(Ti,Nb) or (Hf,Zr)]) for each cluster. For the uniform elemental distribution case, f_{LFC} would equal 0.5 for both ([(Ti,Zr) or (Hf,Nb)] and [(Ti,Nb) or (Hf,Zr)]). However, as shown in Fig. 7(e), the clusters of ([(Ti,Zr) or (Hf,Nb)] are apparently favored over [(Ti,Nb) or (Hf,Zr)]) in the annealed TiZrHfNb samples obtained from CE-based MC simulation (T_{MC} = 400 K – 1800 K). Such compositional fluctuation become extremely pronounced below T_{MC} = 600 K, and finally, f_{LFC} for [(Ti,Zr) or (Hf,Nb)] reaches as high as 0.9 at the lowest T_{MC}.

4. Discussion

4.1. CSRO effect on mechanical deformation

Next, we applied Curtin's solid solution strengthening model [50–52] to predict the yield strength of the RSS versus CSRO TiZrNb-based HEAs. This strengthening theory is an analytic model that assumes that individual solutes interact elastically with dislocations in the average alloy matrix. For an bcc alloy containing n types of alloying components with concentrations c_n, the shear yield stress and energy barrier ΔE_b for thermally activated flow at zero-temperature can be estimated as

$$\tau_{y0} = 0.040\alpha^{-\frac{1}{3}}G\left(\frac{1+\upsilon}{1-\upsilon}\right)^{\frac{4}{3}}\left[\frac{\sum_n c_n \Delta V_n^2}{b^6}\right]^{\frac{2}{3}} \tag{9}$$

$$\Delta E_b = 2.00\alpha^{\frac{1}{3}}Gb^3\left(\frac{1+\upsilon}{1-\upsilon}\right)^{\frac{2}{3}}\left[\frac{\sum_n c_n \Delta V_n^2}{b^6}\right]^{\frac{1}{3}} \tag{10}$$

Here, G, ν represents the shear modulus and Poisson's ratio, respectively. α=1/12 is a weighting factor for the dislocation line tension in bcc lattices. The average Burgers vector b is given as $b = \sqrt{3}/2a_0$, with a_0 denotes the lattice constant of bcc TiZrNb-based HEAs. ΔV_n is the atomic misfit volume for the type-n element, which can be determined as [53]

$$\Delta V_n = \sum_m c_m \langle \Delta V^{n/m}\rangle \tag{11}$$

where $\langle \Delta V^{n/m}\rangle$ reflects the volume change induced by randomly substituting type-m atom with type-n atom. Then, the predicted yield stress τ_y at finite temperature T and finite strain rate $\dot{\epsilon}$ can be expressed as

$$\tau_y = 3.06\tau_{y0}\left[1-\left(\frac{kT}{\Delta E_b}\ln\frac{\dot{\epsilon}'_0}{\dot{\epsilon}}\right)^{\frac{2}{3}}\right] \tag{12}$$

Here, $\dot{\epsilon}_0$ = 10^4 s^{-1} is a reference strain rate and 3.06 is the Taylor factor for polycrystals strengths controlled by edge dislocations. The finite strain rate $\dot{\epsilon}$ here is set to 10^{-3} s^{-1}.

For each alloy, we calculated the atomic misfit volume, shear moduli, lattice constant at 0 K for both RSS and CSRO configurations, containing 250 atoms, which are within the computational capacity of DFT calculation. Here, the CSRO configurations were obtained from DFT-based MC simulation (see Methods section for details and our previous simulation for TiZrHfNb [27]). Using Eqs. (9) and (12), the predicted yield strength of both RSS and CSRO configurations are shown in Fig. 8. As seen in Fig. 8(a), for all three TiZrNb-based HEAs CSRO led to a small but noticeable (of the order of ~11%) increase in yield strength. Specifically, the predicted yield strengths of (i) RSS TiZrNb, TiZrHfNb, and TiZrHfNbTa are 521.7, 634, and 787.1 MPa, respectively; (i) CSRO TiZrNb, TiZrHfNb, and TiZrHfNbTa are 598.3, 717 and 834.8 MPa, respectively. Meanwhile, Fig. 8(b) shows a comparison of the experimentally measured and the predicted (both RSS and CSRO) yield strength for these three TiZrNb-based HEAs. Clearly, the predicted yield strengths of the
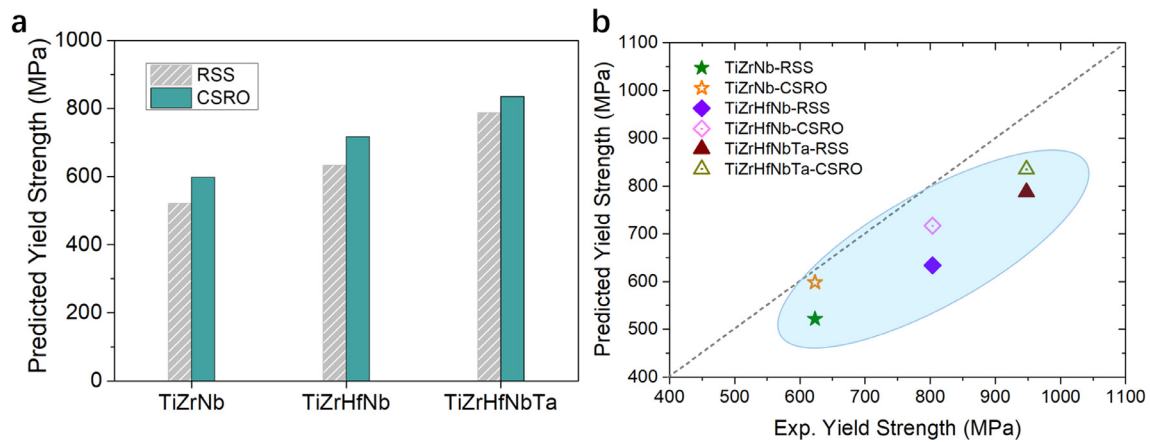
Fig. 8. (a) Predicted yield strength of RSS and CSRO configurations for TiZrNb-based HEAs at 300 K. (b) A comparison of yield strength between the experimental measurement [5,8,10,17,27,54–56] and theoretical prediction for these RSS and CSRO TiZrNb-based HEAs. The dashed line indicates where the predicted yield strength equals to the experimental value.
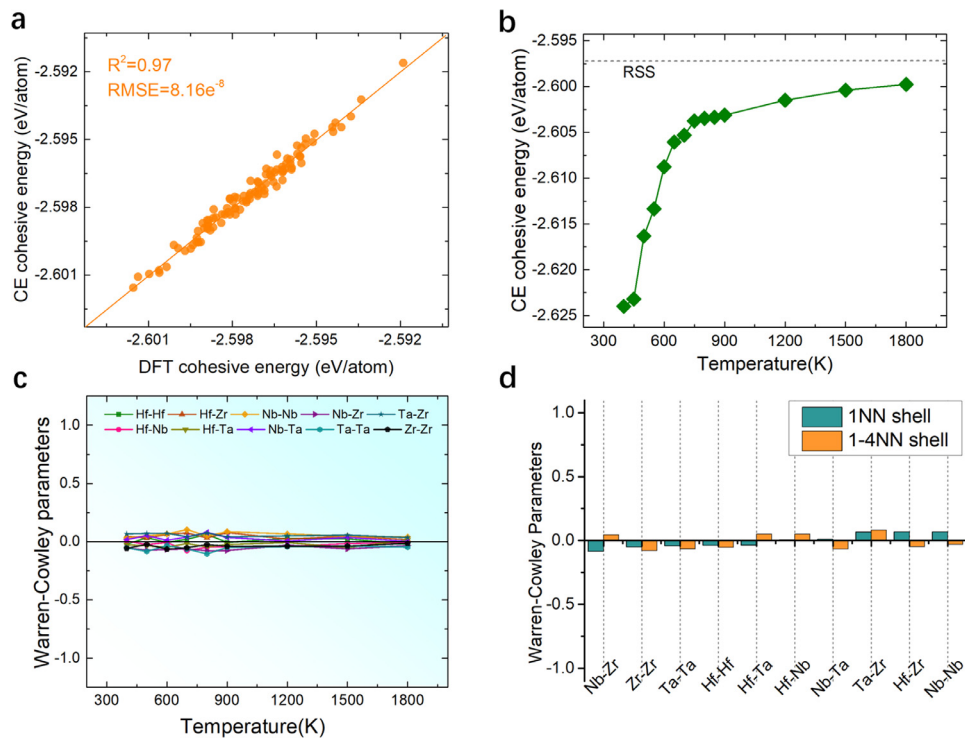

Fig. 9. (a) CE predicted versus DFT calculated cohesive energy of TaZrHfNb alloy. (b) Variations in the cohesive energy of CE-based MC-annealed configurations at different temperatures. (c) Temperature-dependent Warren–Cowley parameters δ_{ij} of the 1 NN shell among different pairs. (d) Histogram of Warren–Cowley parameters δ_{ij} in the 1NN and 1-4 NN shells at $T_{MC} = 400$ K.

RSS samples are generally lower than the experimental values by ~100 MPa, while the predicted yield strengths of corresponding CSRO samples approach the experimental measurements. This indicates the need to take into account the contribution of CSRO (or other local chemical inhomogeneities) to achieve a more accurate prediction of the yield strength of TiZrNb-based bcc HEAs. This is because the experimental HEA samples inevitably contain a certain degree of local chemical inhomogeneity, above and beyond the random solid solutions. Note that our MC-annealed samples (based on DFT calculation) for the predicted yield strength in Fig. 8 only contain CSRO as the sole chemical inhomogeneity. For alloys with local compositional fluctuation, an additional influence could be present on the yield strength and ductility. For example, a recent study of nanocrystalline nickel-cobalt solid solutions [31] showed tensile strengths of approximately 2.3 gigapascals with a respectable ductility of approximately 16% elongation to failure, which is achieved by compositional undulation in a highly concentrated solid solution. Other literature [7,8], including *in situ* transmission electron microscopy experiments in a bcc TiZrHfNb, has also captured evidence that local chemical fluctuations in HEAs could have significant influences on their strength and ductility, from direct observations of the dislocation pinning as well as local double cross-slips caused by the local chemical fluctuation . These studies emphasize a nontrivial effect of local chemical in-

homogeneity (compositional modulation/fluctuation, chemical order from CSRO to LCO on various length scales) on the mechanical behavior and deformation mechanisms of HEAs.

4.2. Effects of substituting Ti with Ta

In addition to the TiZrHf-based alloys discussed above, TaZrHfNb is another bcc refractory HEA with outstanding mechanical properties and has been under recent studies [13,57]. TaZrHfNb, with Ta replacing Ti in TiZrHfNb alloy, can be viewed as a relative of the TiZrNb-based HEAs investigated above. Thus, we have also examined whether local chemical inhomogeneity features are present, in such quaternary HEAs using CE-based MC simulation (same approach as that for TiZrNb-based HEAs in the Methods section). Specifically, as shown in Fig. 9(a), the cohesive energies of CE predicted *vs* DFT calculated are very consistent, with a RMSE of 8.16×10^{-8} eV/atom and a correlation coefficient (R^2) of 0.97, suggesting a satisfactory prediction accuracy. Fig. 9(b) shows the variations in the cohesive energy of the CE-based MC-annealed configurations at different temperatures. As the applied MC temperature decreases from 1800 to 400 K, the cohesive energy decreases by 0.024 eV per atom. However, unlike the TiZrNb-based HEAs, the CSRO characteristics of the 1 NN shell in TaZrHfNb is fairly weak, yielding a very small δ_{ij} for all types of pairs even at the lowest MC temperature, as shown in Fig. 9(c). Moreover, Fig. 9(d) also indicates the low degree of local chemical order for all types of atomic pairs within the 1-4 NN shells at 400 K. This observed weak degree of local chemical order in TaZrHfNb HEA is in stark contrast to those for TiZrNb, TiZrHfNb and TiZrHfNbTa alloys. This discrepancy could originate from the special role of Ti in those TiZrNb-based bcc refractory HEAs. According to the estimated mixing enthalpy by Miedema's model [49] the value of Ta-Zr is 3 kJ/mol, which is high than that of Ti-Zr (0 kJ/mol). Such difference explains the weaker chemical affinity and order tendency of Ta-Zr. As illustrated in Figs. 5 and 6, Ti-Zr pairs exhibit the strongest chemical affinity and ordering tendency. Once Ta replaces Ti, the Ti-induced pronounced chemical order (*i.e.*, the Ti-Zr and Ti-Hf bonds) is no longer present. This leaves Ta, Zr, Nb and Hf almost on equal footing in their competition to form nearest-neighbor pairs. Hence, only a low degree of local chemical order can be formed in the TaZrHfNb HEA.

5. Conclusions

In summary, we have used the cluster expansion approach to systematically uncover the local chemical inhomogeneity in three representative equiatomic TiZrNb-based body-centered cubic refractory HEAs: TiZrNb, TiZrHfNb and TiZrHfNbTa alloys. The chemical inhomogeneities mapped out include local chemical order and compositional undulation, from the nearest neighbor atomic shell up to about one nanometer in length scale.

(1) The local chemical order features in the TiZrNb-based alloys are as follows: (i) For the TiZrNb alloy, the Ti-Zr pair is the most favored, while there exists relatively weaker Nb-Nb pair; (ii) For the TiZrHfNb alloy, Ti and Nb prefer to pair with Zr and Hf, respectively; (iii) For TiZrHfNbTa, Ta is prone to form sub-nanoscale segregation, in addition to the existing chemical preference among Ti, Zr, Hf and Nb.

(2) Accompanying the LCO, there exists compositional undulation in the TiZrHfNb alloy on nanometer scale, arising from the preferred local enrichment of [(Ti, Zr)] or [(Hf, Nb)] CSROs.

(3) The local chemical inhomogeneity evolves strongly with temperature, from the RSS structure at high temperatures to the pronounced tendency of forming chemically favored pairs at low temperatures. The LCO develops beyond the range of CSRO, to a characteristic length scale of at least one nanometer.

(4) The predicted yield strengths of the RSS samples are generally lower than the experimental values by $\sim$ 100 MPa, while those calculated for CSRO-containing samples approach the experimental measurements. This strongly suggests the need to take into account the contribution of CSRO (and/or other local chemical inhomogeneities) to achieve a more accurate prediction of the yield strength of TiZrNb-based bcc HEAs.

(5) When the strong CSRO-promoting Ti is replaced by Ta, the resultant TaZrHfNb alloy is found to contain only a weak degree of local chemical order, unlike the three representative TiZrNb-based HEAs in the present study.

(6) Our work reveals the trend of the chemical inhomogeneities and compositional undulation that would develop as intrinsic features in these TiZrNb-based bcc HEAs. Meanwhile, the CSRO tendency also sheds light on the fertile emergence of (Ti,Zr,O)-complexes that form upon the addition of oxygen/nitrogen into such HEAs to purposely accentuate (sub)nanometer-scale chemical complexes/heterogeneities.

Declaration of Competing Interest

The authors declare that they have no known competing financial interests or personal relationships that could have appeared to influence the work reported in this paper.

References

[1] E.P. George, D. Raabe, R.O. Ritchie, Nat. Rev. Mater. 4 (2019) 515–534.
[2] B. Cantor, I.T.H. Chang, P. Knight, A.J.B. Vincent, Mater. Sci. Eng. A 375-377 (2004) 213–218.
[3] D.B. Miracle, JOM 69 (2017) 2130–2136.
[4] H. Chung, D.W. Kim, W.J. Cho, H.N. Han, Y. Ikeda, S. Ishibashi, F. Körmann, S.S. Sohn, J. Mater. Sci. Technol. 108 (2022) 270–280.
[5] R.R. Eleti, N. Stepanov, N. Yurchenko, D. Klimenko, S. Zherebtsov, Scr. Mater. 200 (2021) 113927.
[6] A. Biesiekierski, J. Lin, K. Munir, S. Ozan, Y. Li, C. Wen, Sci. Rep. 8 (2018) 5737–5749.
[7] Y. Bu, Y. Wu, Z. Lei, X. Yuan, H. Wu, X. Feng, J. Liu, J. Ding, Y. Lu, H. Wang, Z. Lu, W. Yang, Mater. Today 46 (2021) 28–34.
[8] Z. Lei, X. Liu, Y. Wu, H. Wang, S. Jiang, S. Wang, X. Hui, Y. Wu, B. Gault, P. Kontis, D. Raabe, L. Gu, Q. Zhang, H. Chen, H. Wang, J. Liu, K. An, Q. Zeng, T.G. Nieh, Z. Lu, Nature 563 (2018) 546–550.
[9] B. Schuh, B. Völker, J. Todt, N. Schell, L. Perrière, J. Li, J.P. Couzinié, A. Hohenwarter, Acta Mater. 142 (2018) 201–212.
[10] S. Wang, M. Wu, D. Shu, G. Zhu, D. Wang, B. Sun, Acta Mater. 201 (2020) 517–527.
[11] O. Senkov, J. Scott, S. Senkova, F. Meisenkothen, D. Miracle, C.F. Woodward, J. Mater. Sci. 47 (2012) 4062–4074.
[12] O. Senkov, A. Pilchak, S.J.M. Semiatin, M.T. A, Metall. Mater. Trans. A 49 (2018) 2876–2892.
[13] X. Huang, L. Liu, X. Duan, W. Liao, J. Huang, H. Sun, C. Yu, Mater. Des. (2021) 202.
[14] B. Feng, M. Widom, Mater. Chem. Phys. 210 (2018) 309–314.
[15] Y. Huang, J. Gao, S. Wang, D. Guan, Y. Xu, X. Hu, W.M. Rainforth, Q. Zhu, I. Todd, J. Alloys Compd. 903 (2022) 163796.
[16] S.-P. Wang, E. Ma, J. Xu, Intermetallics 107 (2019) 15–23.
[17] O.N. Senkov, J.M. Scott, S.V. Senkova, D.B. Miracle, C.F. Woodward, J. Alloys Compd. 509 (2011) 6043–6048.
[18] S. Wei, S.J. Kim, J. Kang, Y. Zhang, Y. Zhang, T. Furuhara, E.S. Park, C.C. Tasan, Nat. Mater. 19 (2020) 1175–1181.
[19] H. Song, F. Tian, Q.-M. Hu, L. Vitos, Y. Wang, J. Shen, N. Chen, Phys. Rev. Mater. 1 (2017) 023404.
[20] Y. Tong, S. Zhao, H. Bei, T. Egami, Y. Zhang, F. Zhang, Acta Mater. 183 (2020) 172–181.
[21] B. Gludovatz, A. Hohenwarter, K.V. Thurston, H. Bei, Z. Wu, E.P. George, R.O. Ritchie, Nat. Commun. 7 (2016) 10602.
[22] F.X. Zhang, S. Zhao, K. Jin, H. Xue, G. Velisa, H. Bei, R. Huang, J.Y.P. Ko, D.C. Pagan, J.C. Neuefeind, W.J. Weber, Y. Zhang, Phys. Rev. Lett. 118 (2017) 205501.

[23] J. Ding, Q. Yu, M. Asta, R.O. Ritchie, Proc. Natl. Acad. Sci. U. S. A. 115 (2018) 8919–8924.
[24] R. Zhang, S. Zhao, J. Ding, Y. Chong, T. Jia, C. Ophus, M. Asta, R.O. Ritchie, A.M.J.N. Minor, Nature 581 (2020) 283–287.
[25] X. Chen, Q. Wang, Z. Cheng, M. Zhu, H. Zhou, P. Jiang, L. Zhou, Q. Xue, F. Yuan, J. Zhu, X. Wu, E. Ma, Nature 592 (2021) 712–716.
[26] Q. Ding, Y. Zhang, X. Chen, X. Fu, D. Chen, S. Chen, L. Gu, F. Wei, H. Bei, Y. Gao, M. Wen, J. Li, Z. Zhang, T. Zhu, R.O. Ritchie, Q. Yu, Nature 574 (2019) 223–227.
[27] J. Pang, H. Zhang, L. Zhang, Z. Zhu, H. Fu, H. Li, A. Wang, Z. Li, H. Zhang, J. Mater. Sci. Technol. 78 (2021) 74–80.
[28] E. Ma, X. Wu, Nat. Commun. 10 (2019) 1–10.
[29] Y. Wu, F. Zhang, X. Yuan, H. Huang, X. Wen, Y. Wang, M. Zhang, H. Wu, X. Liu, H.J. Wang, J. Mater. Sci. Technol. 62 (2021) 214–220.
[30] J. Ding, Z.J. Wang, Acta Metall. Sin. 57 (2021) 413–424.
[31] H. Li, H. Zong, S. Li, S. Jin, Y. Chen, M.J. Cabral, B. Chen, Q. Huang, Y. Chen, Y. Ren, K. Yu, S. Han, X. Ding, G. Sha, J. Lian, X. Liao, E. Ma, J. Sun, Nature 604 (2022) 273–279.
[32] Q.J. Li, H. Sheng, E. Ma, Nat. Commun. 10 (2019) 1–11.
[33] B. Zhang, J. Ding, E. Ma, App. Phys. Lett. 119 (2021) 201908.
[34] V. Blum, G.L.W. Hart, M.J. Walorski, A. Zunger, Phys. Rev. B 72 (2005) 165113.
[35] A. van de Walle, Calphad 33 (2009) 266–278.
[36] M. Ångqvist, W.A. Muñoz, J.M. Rahm, E. Fransson, C. Durniak, P. Rozyczko, T.H. Rod, P. Erhart, Adv. Theory Simul. 2 (2019) 1900015.
[37] A.v.d. Walle, M. Asta, Model. Simul. Mater. Sci. Eng. 10 (2002) 521–538.
[38] J.M. Sanchez, Phys. Rev. B 81 (2010) 224202.
[39] A. Fernández-Caballero, J.S. Wróbel, P.M. Mummery, D. Nguyen-Manh, J. Phase Equilibria Diffus. 38 (2017) 391–403.
[40] G. Kresse, J. Hafner, Phys. Rev. B-Condens. Matter. 47 (1993) 558–561.
[41] G. Kresse, J. Hafner, Phys. Rev. B Condens. Matter. 49 (1994) 14251–14269.
[42] H.J. Monkhorst, J.D. Pack, Phys. Rev. B 13 (1976) 5188–5192.
[43] P.E. Blöchl, Phys. Rev. B 50 (1994) 17953–17979.
[44] John P. Perdew, Kieron Burke, Matthias Ernzerhof, Phys. Rev. Lett. 77 (1996) 3865–3868.
[45] A. van de Walle, P. Tiwary, M. de Jong, D.L. Olmsted, M. Asta, A. Dick, D. Shin, Y. Wang, L.Q. Chen, Calphad 42 (2013) 13–18.
[46] A. Tamm, A. Aabloo, M. Klintenberg, M. Stocks, A. Caro, Acta Mater. 99 (2015) 307–312.
[47] J.M. Cowley, Phys. Rev. 77 (1950) 669–675.
[48] E. Antillon, C. Woodward, S.I. Rao, B. Akdim, Acta Mater. 215 (2021) 117012.
[49] A. Takeuchi, A.J.M. Inoue, Mater. Trans. 46 (2005) 2817–2829.
[50] B. Yin, F. Maresca, W.A. Curtin, Acta Mater. 188 (2020) 486–491.
[51] F. Maresca, W.A. Curtin, Acta Mater. 182 (2020) 235–249.
[52] C. Varvenne, A. Luque, W.A. Curtin, Acta Mater. 118 (2016) 164–176.
[53] B. Yin, W.A. Curtin, NPJ Comput. Mater. 5 (2019) 1–7.
[54] Y.D. Wu, Y.H. Cai, T. Wang, J.J. Si, J. Zhu, Y.D. Wang, X.D. Hui, Mater. Lett. 130 (2014) 277–280.
[55] J.P. Couzinié, L. Lilensten, Y. Champion, G. Dirras, L. Perrière, I. Guillot, Mater. Sci. Eng. A 645 (2015) 255–263.
[56] G. Dirras, L. Lilensten, P. Djemia, M. Laurent-Brocq, D. Tingaud, J.P. Couzinié, L. Perrière, T. Chauveau, I. Guillot, Mater. Sci. Eng. A 654 (2016) 30–38.
[57] S. Maiti, W. Steurer, Acta Mater. 106 (2016) 87–97.